Article Title

T. Nonnenmacher[1]*, T.S. Dascalu[1]*, R. Bingham[2], C.L. Cheung[1], H.T. Lau[1], K. Long[1], J. Pozimski[1], C. Whyte[2]

1 Department of Physics, Imperial College London, Exhibition Road, London, SW7 2AZ, UK;
2 Department of Physics, SUPA, University of Strathclyde, 16 Richmond Street, Glasgow, G1 1XQ, UK;
* Correspondence: toby.nonnenmacher14@imperial.ac.uk, t.dascalu19@imperial.ac.uk

Abstract

An electron plasma lens is a cost-effective, compact, strong-focusing element that can ensure efficient capture of low-energy proton and ion beams from laser-driven sources. A Gabor lens prototype was built for high electron density operation at Imperial College London. The parameters of the stable operation regime of the lens and its performance during a beam test with 1.4 MeV protons are reported here. Narrow pencil beams were imaged on a scintillator screen 67 cm downstream of the lens. For several settings, the lens converted the pencil beams into rings that show position-dependent shape and intensity modulation. Characterisation of the focusing effect suggests that the plasma column exhibited an off-axis rotation similar to the $m = 1$ diocotron instability. The instability was further associated with the formation of rings using particle tracking simulations.

1. Introduction

One of the principal challenges that must be addressed to deliver high-flux pulsed proton or positive-ion beams is the efficient capture of the ions ejected from the source. A typical source produces protons with kinetic energies of approximately 60 keV [1–3] and ions with kinetic energies typically below 120 keV [4,5]. At this low energy the mutual repulsion of the ions causes the beam to diverge rapidly. Capturing a large fraction of this divergent flux therefore requires a focusing element of short focal length. Proton- and ion-capture systems in use today employ magnetic, electrostatic, or radio frequency quadrupoles, or solenoid magnets to capture and focus the beam [2,6–8].

Laser-driven proton and ion sources are disruptive technologies that offer enormous potential to serve in future high-flux, pulsed beam facilities [9–16]. Possible applications include proton-

and ion-beam production for research, particle-beam therapy, radio-nuclide production, and ion implantation. Recent measurements have demonstrated the laser-driven production of large ion fluxes at kinetic energies in excess of 10 MeV [17–20]. The further development of present technologies and the introduction of novel techniques [21,22] makes it conceivable that significantly higher ion energies will be produced in the future [23–25]. By capturing the laser-driven ions at energies two orders of magnitude greater than those pertaining to conventional sources, it will be possible to evade the current space-charge limit on the instantaneous proton and ion flux that can be delivered. However, laser-driven ion beams are highly divergent making it necessary to use a strong-focusing element to capture the beam as close as possible to the ion-production point.

An attractive approach to providing the strong-focusing element required to capture the low-energy (~ 15 MeV) ion flux produced in the laser-target interaction is to exploit the strong focusing forces that can be provided by a cloud of electrons trapped within a cylindrical volume by crossed electric and magnetic fields. Such an electron-plasma lens was initially proposed by Gabor in 1947 [26]. The use of electron-plasma lenses of the Gabor type to capture and focus proton and ion beams has been studied by a number of authors [27–33]. Such a lens has the potential to decrease the magnetic field required in the first focusing element by a factor of more than 40 compared with that required for a conventional beam-capture solenoid of the same focusing strength [34]. For example, for a 25 MeV proton beam, in order to achieve a focal length of 1 m, the required field is 0.06 T for a 0.3 m Gabor lens, in contrast with 2.6 T for a solenoid with the same effective length. This is particularly important when beams are produced with a large divergence angle [35]. The Gabor lens is therefore the ideal focusing element by which to capture a laser-accelerated proton or ion beam. Its compactness and relatively low price are key if it is to be exploited in particle beam therapy facilities. Furthermore, it has been shown in simulation that a Gabor-lens-based system is capable of capturing laser-generated proton beams at energies as high as 250 MeV, the energy required to serve a proton-beam therapy facility [13].

Following the initial proposal by Gabor, several groups have reported stable operation of a space-charge lens under a variety of electrode and magnetic field configurations [27–29,36,37]. Experiments with ion beams confirmed the focusing capability of the Gabor lens and observed beam emittance growth [29,33,38]. The mechanism for electron production and the inhomogeneity in the electron density within the lens were believed to cause the observed growth in emittance [38].

The focusing strength of a Gabor lens is determined by the electron density. The theoretical maximum electron density is related to the electric and magnetic field strength [25]. Careful design of the field configuration allowed certain lenses to operate at electron densities of 61% of the theoretical maximum [34]. At high pressures, the electrons are lost due to the radial expansion of the plasma driven by collisions with neutral atoms. At low pressures, this radial transport can be caused by small

azimuthal asymmetries in the applied electric or magnetic fields [37]. Further work was directed towards the design of an electrostatic lens for the space-charge-compensated transport of a high intensity heavy ion beam [39]. In this case, the absence of emittance growth due to the lens was reported [39].

Advances in simulation and finite-element analysis have been exploited to calculate the expected focusing strength of a space-charge lens and to study the resulting phase-space transformation on a beam passing through the lens. Good agreement between experimental results and beam-transport simulations [33,34] suggest that plasma instabilities are a likely cause of beam aberrations. Experimental observations and numerical results [40] have confirmed that the confined plasma is vulnerable to the diocotron instability [41]. Further studies are required to characterise the configurations under which a Gabor space-charge lens operates in a stable regime.

Plasma-lens focusing for electron beams is being developed by the CERN Linear Electron Accelerator for Research (CLEAR) collaboration [42]. Evidence of aberrations in the CLEAR lens due to radial non-uniformity of the plasma temperature have successfully been demonstrated [43,44]. Previous work at the Stanford Linear Accelerator Center (SLAC) demonstrated the plasma-lens focusing of 28.5 GeV electron [45] and positron [46] beams. Numerical simulations were able to describe the observed non-linear focusing force in this experiment [47]. Discharge-capillary active plasma lenses were also investigated as a compact device for focusing 100 MeV-level electron beams produced by a jet-based laser-plasma accelerator, showing both weak and strong chromatic effects [48] and potential emittance degradation [49]. Research at the University of Oslo seeks to demonstrate the possibility of using such a plasma lens for staging in plasma wakefield acceleration or in radially symmetric final focusing for linear colliders [50]. As compact and tunable devices, active plasma lenses [51,52] are a promising solution for the extraction and transport of the witness bunch while removing the driver without loss of beam quality [53–55]. Finally, electron plasmas were studied in multicell traps [56,57] to develop methods that could increase the number of accumulated positrons compared to the present limits for long-term confinement.

In this paper we report the performance of a Gabor lens prototype constructed at Imperial College London. The lens was exposed to 1.4 MeV protons at the Surrey Proton Beam Centre [58]. The effect on the beam is presented and compared to the results of a simulation of the impact of plasma instabilities on the focusing forces produced by the lens.

2. The Gabor Lens

A schematic of the prototype Gabor lens is shown in figure 1. The total length of the lens, from end flange to end flange, was 540 mm. The central anode was formed of a copper cylinder with an

inner diameter of 85.7 mm and a length of 444 mm. The copper cylinder was 11.5 mm thick and had four rows of four 10 mm diameter holes forming lines along the axis of the cylinder spaced by 90° so that the volume inside the anode would be evacuated efficiently. Two ceramic isolating spacers were used to maintain the position of the central high-voltage electrode and to electrically isolate it from the vacuum tube. A 15 mm copper high-voltage connector was soldered to the central electrode to provide a socket for the high-voltage feed-through designed for voltages up to 60-65 kV.

The two end electrodes were formed of two copper cylinders with a length of 34 mm, an inner diameter of 66.7 mm, and a wall thickness of 1.6 mm. The ends of the cylinders were manufactured with rounded edges to reduce the likelihood of sparking, with a minimum gap of 16.8 mm to the high-voltage anode. The end electrodes were press fitted into the mild steed end flanges. The outer tube and end flanges were connected to ground voltage.

The configuration of the pancake coils is shown in figure 1. The input and output tails of the coils exited through the 50 mm gap in the outer tube of the lens. A water cooled copper conductor was used with a square cross-sectional area of 10.87 mm^2. The base configuration of the coil included four windings. Additionally, the number of windings was locally increased to seven at specific positions to generate a more uniform magnetic field. A maximum magnetic field of approximately 55 mT was achieved at 45 A,

A power supply (Glassman LP 60-46) was used to regulate the current that flows through the coil. Typical values for the current were in the range of 14 A to 30 A. The voltage for the central electrode was provided by a high-voltage supply of the type Glassman Series FR with typical values between 8 kV and 20 kV.

The pumping system was comprised of a roughing pump (Edwards 5) and a turbo molecular pump (Leybold Turbovac 151) with a pressure gauge (Leybold Penninvac PTR 90 N) and a pressure gauge monitor (Leybold Graphix One). The lowest pressure achieved with the lens was 3×10^{-7} mbar, with pressure values being observed up to 3×10^{-5} mbar when a non-neutral plasma was established inside the lens. In the range of 10^{-7} mbar, the operation regime that lead to a stable plasma could be clearly distinguished from the lens settings associated with an unstable plasma. For higher pressures, this distinction was more difficult to be observed.

Plasma in the lens was produced by increasing the high voltage applied to the anode and the current in the magnetic coils. Comparison with simulation demonstrated that a high electron density of around 5×10^{-7} Cm^{-3} was produced.
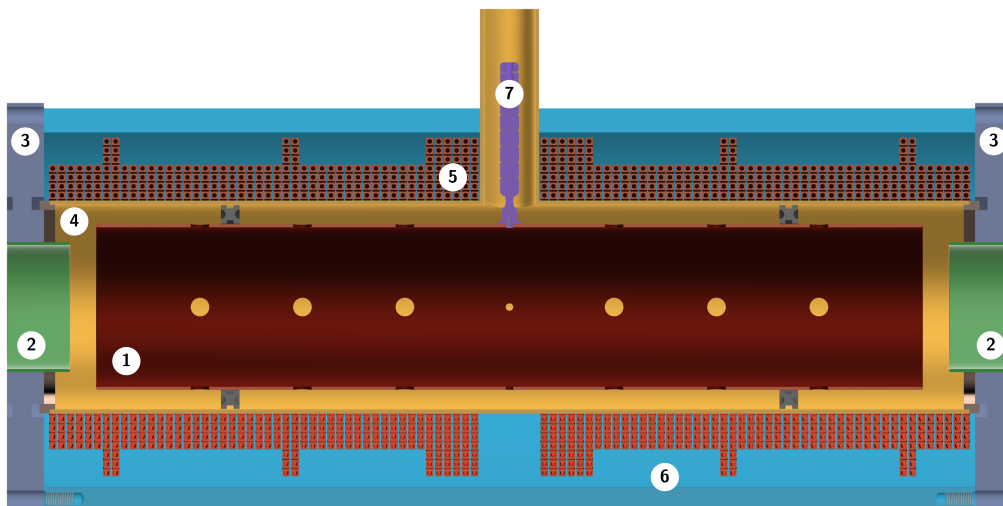
Figure 1. Internal structure of the IC Gabor lens viewed in longitudinal cross-section. The main components are: 1-central anode, 2-end electrodes, 3-end flanges, 4-vacuum tube, 5-pancake coils, 6-outer tube, 7-high-voltage feed-through.

3. Plasma Characterisation

The operation of the lens was tested over the range of available anode voltages and coil currents to identify the regime for which a stable plasma could be produced. Measurements of the plasma in the lens were made using the Medusa voltage sensor shown in figure 2. The sensor detects the current of ions and electrons discharged by the lens. This detector was composed of 16 equal segments with a total area of 122.5 mm^2. The detector segments were connected either in concentric circles or in a sector arrangement, with four segments combined and fed into one channel of an oscilloscope. The Medusa detector was used to measure the range of high voltage and current settings which would produce a stable plasma within the lens. A schematic diagram of the experimental setup for these primary studies is given in Figure 3. For a constant current through the coils of the lens, producing a constant magnetic field, the high voltage was increased from zero until plasma was produced in the lens. The presence of a stable plasma in the lens was indicated by a steady voltage read from the Medusa detector. The high voltage was then increased further, until instability in the plasma, characterised by sparking, was observed as an extreme variation in the output voltage reading.

Figure 4 shows the amplitude responses observed in the Medusa detector that are typical of three modes of operation:

- *Plasma off*: high voltage and current through coils below the threshold for plasma to be produced;
- *Stable plasma*: plasma produced with high voltage below 25 kV and current below 27 A; and
- *Unstable plasma*: plasma produced with higher magnetic field causing considerable sparking and therefore large variations in the output amplitude.
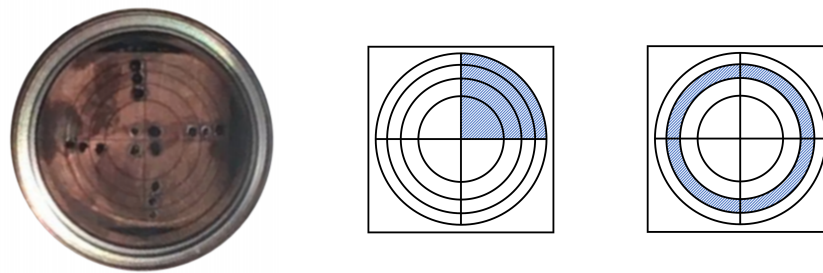
Figure 2. The segmented detector used for measuring the current of electrons and ions exiting the Gabor Lens. The detector is divided in to 16 sections of equal area which were combined in sector (middle) or concentric circle (right) arrangements.
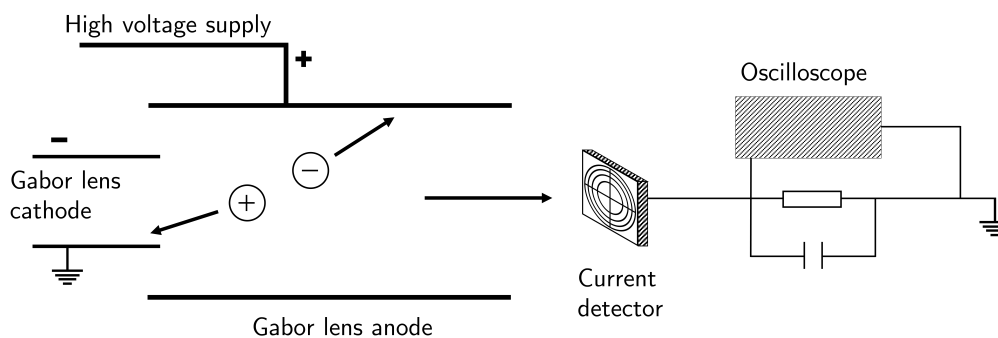

Figure 3. Schematic of the Gabor lens, current detector, and oscilloscope. The high voltage supply maintains the drop across the electrodes. Expelled ions hit the detector, and the current signal is converted to a voltage output signal in the oscilloscope.

The frequency spectrum of the three modes of operation shows a non-negligible amplitude only at low frequency for the unstable plasma signal.

The mean and standard deviation of the different plasma regions are shown in table 1. The mean increases slightly, when the plasma is switched on, while the standard deviation remains largely unchanged. As the current applied through the coils becomes too large, and the unstable region is reached, the mean and standard deviation rise and a large amount of noise is seen. This is shown in figure 4, where the level of noise is very similar with the plasma off and on, and only increases appreciably upon reaching the unstable region. In this region, the low frequency noise is increased significantly, while the high frequency noise remains largely unchanged. The operation regime described in this section had been used to verify that the lens produced a stable plasma during the beam test.

4. Beam Test Setup

The prototype Gabor lens was exposed to proton beams with a kinetic energy of 1.4 MeV at the Ion Beam Facility at the University of Surrey [58] in October 2017. Schematic diagrams of the two setups used in the beam tests are shown in figure 5. The proton beam entered the lens through a section of
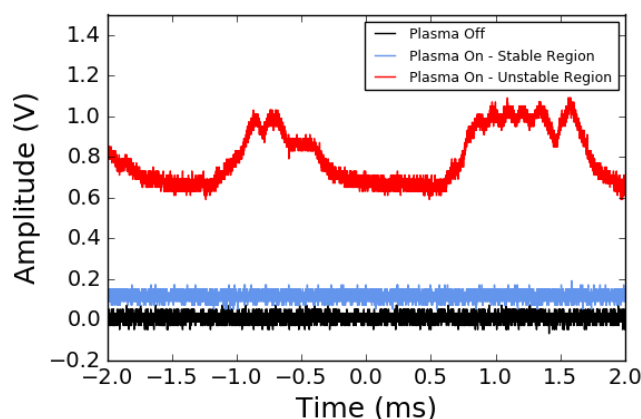
Figure 4. Amplitude of signal from the Medusa detector in three regions: plasma off, plasma on, and plasma on in unstable region. The time range is given $0.0004\,\text{s}$, and the time resolution of the measurement is $4 \times 10^{-7}\,\text{s}$. The voltage range is $0.5\,\text{V}$ with a resolution of $0.01\,\text{V}$.

Table 1. Mean and Standard Deviation values for Plasma Off, On, and Unstable regions shown in figure 4.

	Mean (V)	Standard Deviation (V)
Plasma Off	0.008	0.019
Plasma On	0.114	0.020
Plasma Unstable	0.797	0.133

evacuated beam pipe. The length of the drift on the first day of data taking was approximately $380\,\text{mm}$ (Setup 1 in figure 5). On the second day the length of the drift was extended to approximately $680\,\text{mm}$ to exploit the divergence of the beam to illuminate a larger area at the front face of the lens (Setup 2 in figure 5).

Narrow "beamlets" were created using an aperture plate placed at the entrance to the lens (see figure 6). The holes in the aperture plate were $2\,\text{mm}$ in diameter and arranged in a pattern designed to minimise the overlap of the outgoing beamlets under a focusing force that is rotationally symmetric about the beam axis.

A further section of evacuated beam pipe of length $670\,\text{mm}$ was attached to the downstream flange of the prototype lens. A phosphor screen was installed on the downstream flange as indicated in figure 5. The phosphor screen used was a P43 phosphor surface on an aluminized pyrex substrate with an effective area of diameter $44.9\,\text{mm}$ and a thickness of $10\text{-}15\,\mu\text{m}$. Photographs of the image of the beam on the phosphor screen were acquired with a DSLR camera using an exposure long compared to the beam spill.
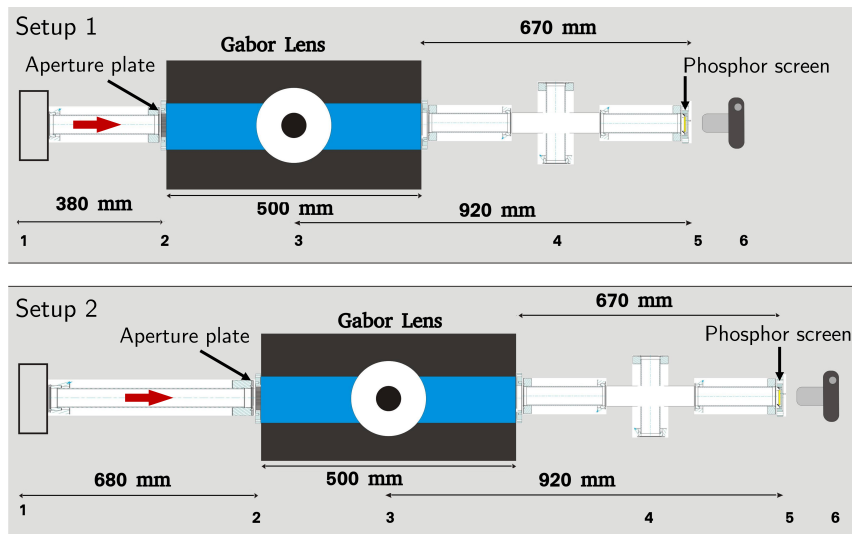
Figure 5. Schematics of the day 1 beam test setup, Setup 1 (top) and the day 2 beam test setup, Setup 2 (bottom). The setup includes the Gabor lens, aperture, and beam pipes.
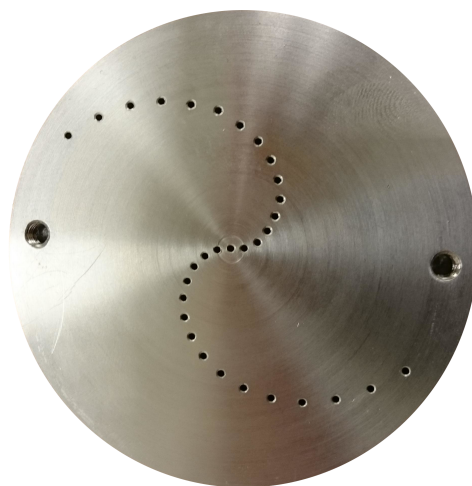

Figure 6. Photograph of the aperture placed in the beamline upstream of the Gabor Lens. 30 holes of 2 mm width are drilled in a symmetrical pattern around one further hole on the axis. The surrounding holes are pitched at an angle of $20°$.
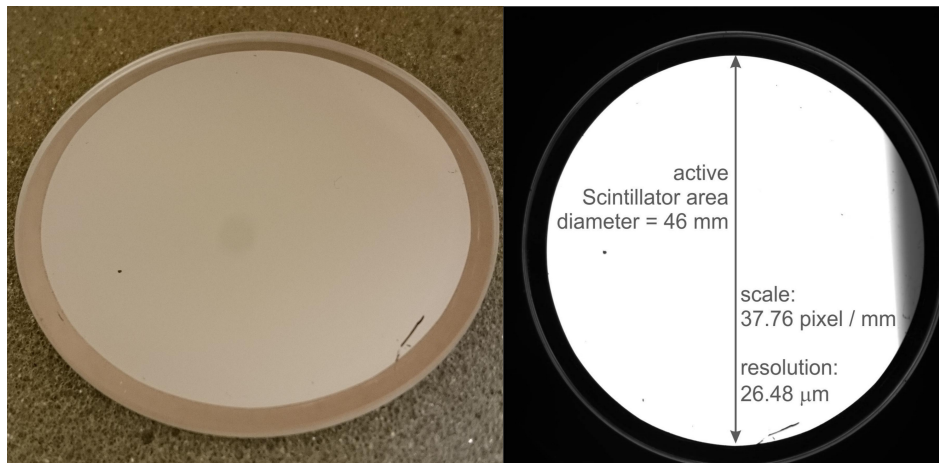
Figure 7. Photograph and schematic of the phosphor screen used for imaging the beam. The screen was composed of a P43 phosphor surface on a substrate of aluminized pyrex, and the scale and resolution of the screen are shown on the schematic.

5. Characterisation of lens performance

The lens was set up on the beam line and operation of the lens was re-established as described in section 3. The voltage-current characteristics of the lens measured using the Medusa detector with the lens on the beam line are compared with those measured at Imperial in figure 8. The two sets of measurements show similar features indicating that the lens was operating in a similar manner to the initial lab test. Thus, figure 8 acted as an indication of the approximate regime where an electron plasma was formed in the lens.

Images of beam impinging on the phosphor screen were taken with the lens turned off in both the Setup 1 and Setup 2 configurations (see figure 9). Distinct "spots" are visible that correspond to the beamlets produced by the holes in the aperture plate. The longer drift introduced in the Setup 2 configuration results in a larger number of beamlets being observed at lower magnification than in the Setup 1 configuration. The central axis of the lens passes through the centre of the second beamlet from the right in both Setup 1 and Setup 2. Measurement of the diameter of the beam spots and the centre-to-centre distances allowed the divergence of the beam to be determined. The divergence in the x and y directions was determined to be $x' = 1.6\,\text{mrad}$ and $y' = 0.5\,\text{mrad}$, respectively.

Images of the beam with the lens operating at a voltage of 20 kV are shown for currents of 28 A and 33 A in figure 10. The figure shows that the effect of the lens is to produce ring-like structures on the phosphor screen. The diameter and eccentricity of the rings increases with radial distance from the beam axis. The brightness of the image is observed to vary around the ring. This effect is seen more clearly in figure 11 which shows the intensity distribution plotted as a function of position on the phosphor screen. The ring-like structure of the beam spots is clearly visible against the low background and the non-uniformity of the intensity distribution is also observed. The integrated intensity as well
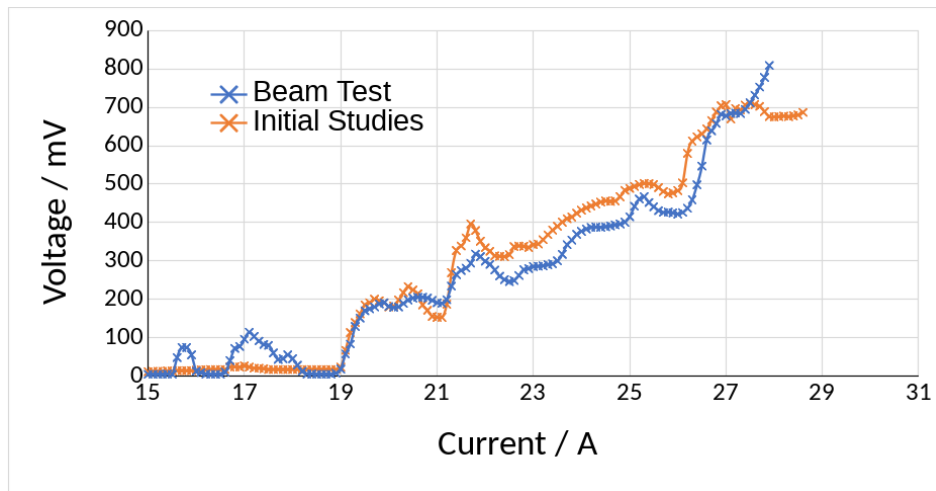
Figure 8. Voltage-current characteristic of the Gabor lens measured with the lens on the beam line (blue crosses) compared to measurements in the laboratory at Imperial (orange crosses). During the beam test the gas pressure in the lens was 10% higher than the pressure at which the lens operated in the laboratory.
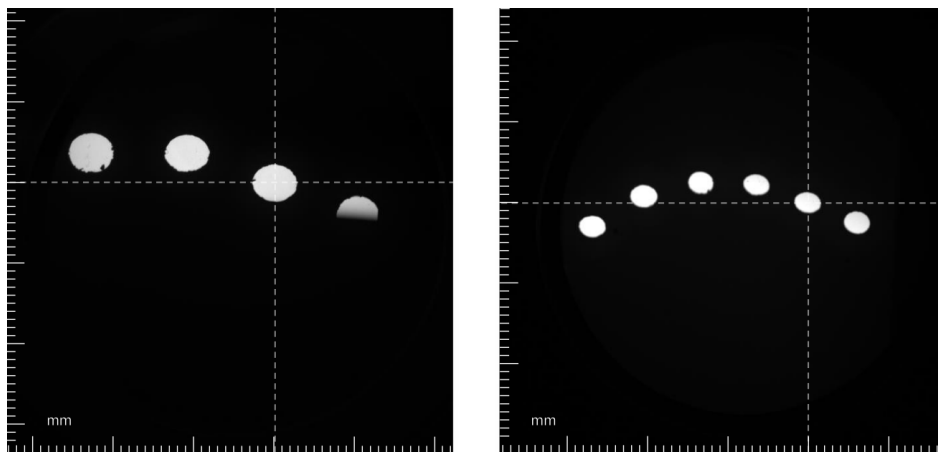

Figure 9. Observed camera image of the 3 beam spots beyond the aperture in the Setup 1 configuration, left, and with 6 beam spots beyond the aperture in the Setup 2 configuration, right. Both images were taken with the lens off. The dashed lines indicate the beam axis and the central beam spot.
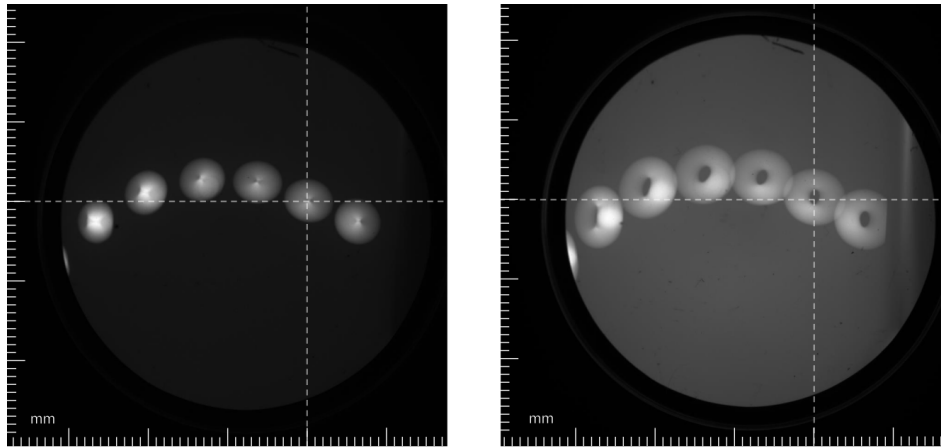
Figure 10. Observed camera image of the 6 beam spots beyond the aperture in the Setup 2 configuration with the lens on at a current through the coils of 28 A, left and 33 A, right. Both images were taken with a lens voltage of 20 kV. An additional spot is visible on the left hand side, as the lens focusing is increased. The dashed lines indicate the beam axis.

as the intensity distribution around the ring differs from ring to ring. Similar behaviour has previously been reported in [59,60].

To understand the distribution of the space-charge inside the lens better and the plasma dynamics during the beam test, a particle-in-cell (PIC) code VSIM [61] was used to identify the main characteristics of a plasma instability that converts pencil beams into rings. The protons were propagated through the electron plasma using VSIM for a number of plasma instabilities that had been observed experimentally [62,63]: a hollow electron ring and the diocotron instability [64]. The diocotron modes observed in the simulations corresponded to higher modes with an azimuthal mode number m > 1. Within the range of electron densities between 1×10^{13} m^{-3} and 1×10^{15} m^{-3}, no ring formation was observed in the simulations. The instabilities named above have good azimuthal symmetry during their evolution and, hence, focus the pencil beams at the same position at all times. A displacement of the bulk of the plasma from the central axis and the rotation of the focusing centre are necessary for the formation of rings. An example of such an instability is shown in figure 12 and consists of a region of high electron density and a region of low electron density that rotate around the beam axis. Figure 12 shows the result of tracking six proton pencil beams through the instability. Rings are formed on a screen downstream of the lens. As the instability is gradually damped and the bulk of the plasma approaches the central axis, each pencil beams is focused on a ring with a radius that decreases and a centre that shifts with time, thus, producing a set of overlapped rings.

In parallel, a particle-tracking code, BDSIM [65], was used to simulate the formation of the rings on a screen downstream of the lens for a simplified plasma distribution that reproduces the main features of the m = 1 diocotron mode. The non-neutral plasma was modelled as a longitudinal column of electrons with azimuthal symmetry. The central axis of the column is displaced from the beam axis and
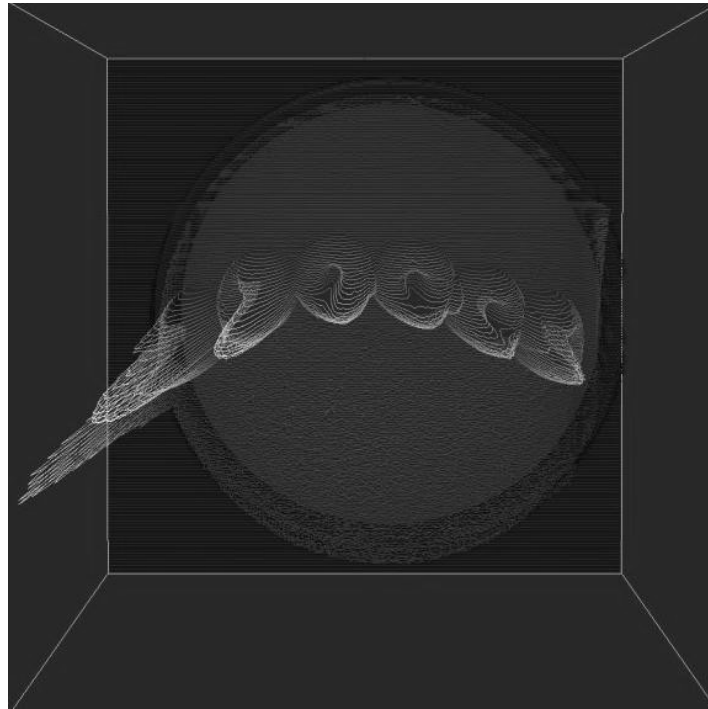
Figure 11. 3D plot of the scintillator measurement of the 6 beam spots in the Setup 2 configuration, with the lens on. The image is shown looking down along the beam axis.
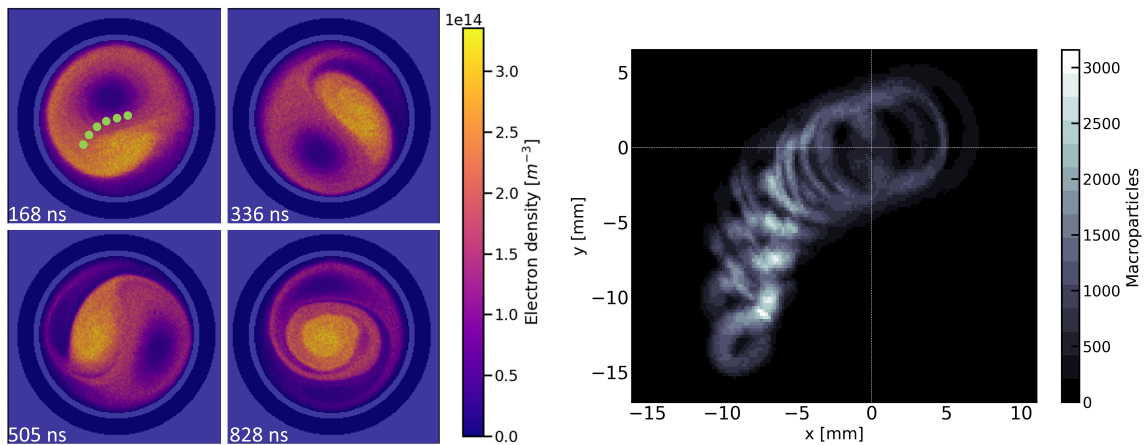

Figure 12. PIC [61] simulation of a plasma instability that was observed to focus the proton pencil beams into rings. Left: The averaged density of plasma in a transverse cross-section through the lens at four different time steps during the evolution of the instability. The green spots mark the entry position of the pencil beams. Right: Number of macroparticles hitting a screen 67 cm downstream of the lens.
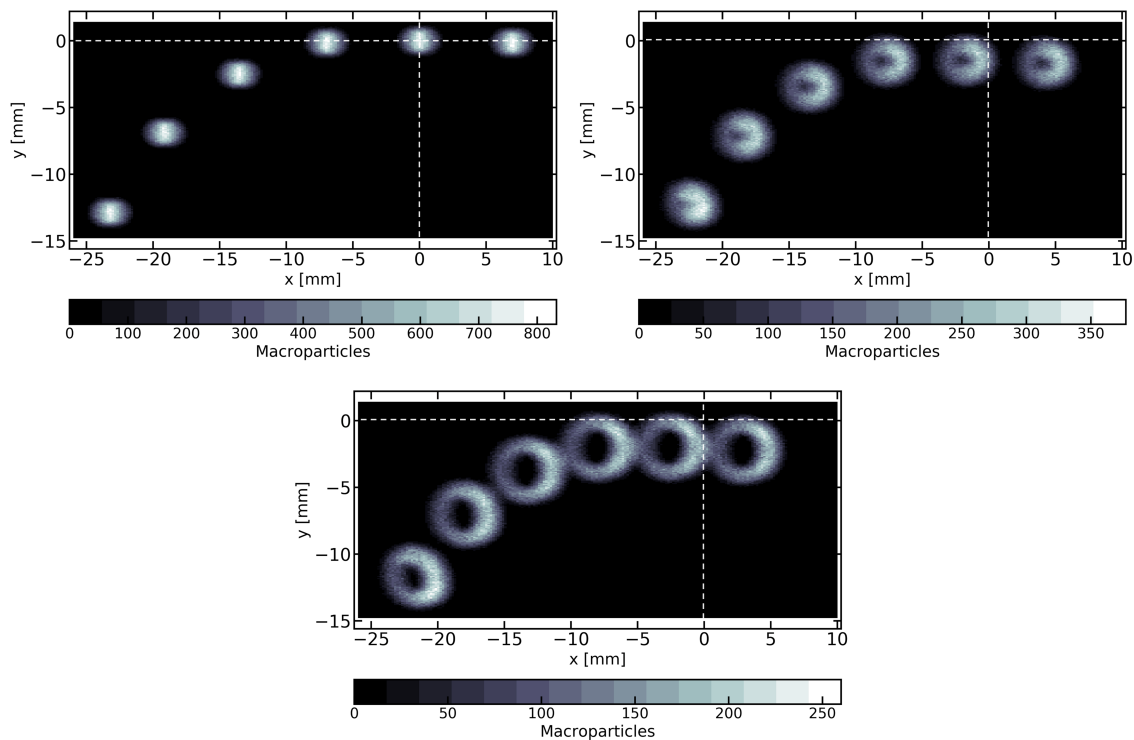
Figure 13. The effect of a plasma column rotating around the beam axis on six proton pencil beams as simulated with BDSIM [65] for electron densities of $0\,\mathrm{m}^{-3}$, $1.8 \times 10^{14}\,\mathrm{m}^{-3}$, and $2.8 \times 10^{14}\,\mathrm{m}^{-3}$. Increasing the density of the plasma modifies the separation and the width of the rings. The plasma column has a radius $r_c = 14\,\mathrm{mm}$ and an offset $D = 7\,\mathrm{mm}$ from the central axis of the lens.

rotates around it with a constant period that is larger than the transit time of the protons through the lens. The electron cloud has a region of constant density in the centre and a negative radial gradient up to the walls of the lens anode. The six proton pencil beams were tracked through the lens using a time dependent electric field map and a static magnetic field map generated from the space-charge distribution and a model of the coil, respectively. The initial phase-space of the protons upstream of the lens was tuned such that the intensity profile of the pencil beams on the screen obtained from the simulation matches the images taken during the beam test with the lens off.

Figure 13 shows the focusing effect of a rotating plasma column on the pencil beams as a result of the particle tracking. A variation of the separation between the rings and the width of each ring is seen as a function of the density of the plasma. The shape and thickness of the rings are influenced by changes in the electron density and in the radius of rotation of the plasma column. The eccentricity of the rings increases for the pencil beams that are further away from the beam axis as a result of the different focusing strengths in the x and y directions. This geometrical effect depends on the relative position of the pencil beam with respect to the rotation axis of the plasma column. As in the experimental observations, the brightness of each ring is seen to vary along the circumference. The simulations

indicated that the position and extent of the intensity peak is dependent on the ratio between the period of rotation of the plasma column and the transit time of the protons through the lens.

A systematic study of the characteristics of the rings was carried out as a function of the voltage and current settings at which the lens was operated during the beam test. Three parameters were used to characterise the rings:

1. Centroid $\mathbf{r_c} = (x_c, y_c)$: The centroid was taken to be the weighted average of all the pixels constituting a ring above a fixed intensity threshold $(x_c, y_c) = \left(\frac{M_{10}}{M_{00}}, \frac{M_{01}}{M_{00}} \right)$, where M_{ij} are the image moments $M_{ij} = \sum_x \sum_y x^i y^j I(x, y)$ of the pixel intensity $I(x, y)$.
2. Diameter, $\mathcal{D}_{x,y}$: The diameter of the ring (or of the beam spot in images taken with the lens off) was determined along the x and y directions separately. The diameter is defined as the width of a beam spot or ring along the $x-$ or $y-$ direction after an intensity cutoff was applied to a camera image.
3. Eccentricity, $\mathcal{E}$: The eccentricity is defined as the ratio $\frac{\mathcal{D}_x}{\mathcal{D}_y}$.

Applying a pixel intensity cutoff to the images to extract the diameter and centroid position introduces an associated uncertainty. Measuring the parameters above, the calculated uncertainties are $\pm 0.3\,\text{mm}$ for $\mathcal{D}_x$, $\pm 0.2\,\text{mm}$ for $\mathcal{D}_y$, and $\pm 0.05\,\text{mm}$ for x_c and y_c.

A comparison of the effects of electric field only and magnetic field only in the lens is shown in figure 14. This plot presents data from Setup 1, in which the 3 spots are those shown in figure 9, with the rightmost point corresponding to the beam axis centre. Squares and Circles represent variation in current through the magnetic coils only, in simulation and data respectively, with no applied high voltage. Crosses represent variation in high voltage (and therefore electric field) with no current through the magnetic coils. As expected from theoretical consideration, applying only electric potential does not influence the particle transport to a degree comparable with variation from change in magnetic field. Comparison between magnetic field only data and calculated influence of particle transport due to magnetic field shows good agreement in direction as well as magnitude. This is true for all three of the observed pencil beamlets. The small variation around the pencil beam on the beam axis indicates that the beam axis, aperture axis, and lens axis were not identical.

Figure 15 shows the variation in X and Y position of the three beam spot centroids in Setup 1, under the effects of both applied magnetic field and high voltage. In this case, the high voltage is held at $15\,\text{kV}$, while the current through the magnetic coils is varied from 0 to $32\,\text{A}$. An approximately linear increase with magnetic field is observed. Given the expectation that the lens plasma density should increase as the square of the field, this implies an alternative limiting factor: in addition to the force producing circular motion in the lens, there is a force that is constant in time causing an off centre drift. The two sets of data, for $15\,\text{kV}$ and $20\,\text{kV}$, were taken in consecutive days which indicates that the
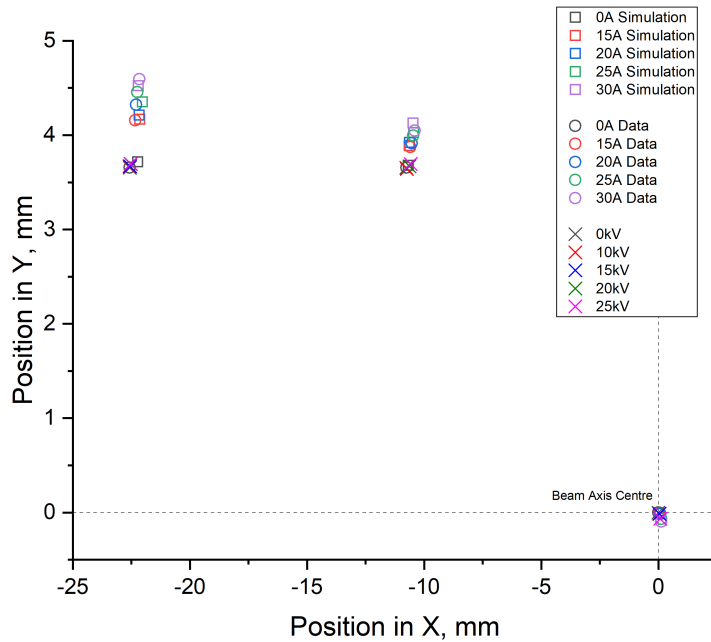
Figure 14. Position of the centroid of the 3 beam spots for varying magnetic fields and high voltages. Data are represented by circles and crosses, while simulated data are represented by squares.

driving mechanism associated with the observed plasma dynamics is a characteristic of the geometry or operation of the lens.

The variation in X and Y diameter of the six beam spots from Setup 2 is given in Figure 16: with a constant applied voltage of 15 kV, the variation in spot diameter with magnetic field is shown. A non-linear increase in spot size with change in magnetic fields is observed, with the rate of increase in diameter getting larger at high magnetic fields. This indicates that the increase in plasma density with magnetic field is larger than linear and, thus, that the plasma trapping efficiency varies with the magnetic field strength. That the points remain within the lines shown, implies that there is a trend for the change in diameter for a given spot. The ratio variation being solely dependent on initial position of spot indicates that this effect is caused by the density distribution of the plasma in the transverse plane.

Figure 17 shows the change in XY ratio of the six beam spots from Setup 2 with variation in magnetic field. The forces in X and Y change to different extents, with an increased difference at greater distances from the beam axis. At those points farther from the beam centre, the force in X is bigger than in Y, indicating that the centre of the lens has a low plasma density, while further from the axis of the lens, the plasma density increases with radius. In addition, there is some perturbation that introduces a time dependency in the motion of the plasma. Figures 14 to 17 may be understood in terms of a position
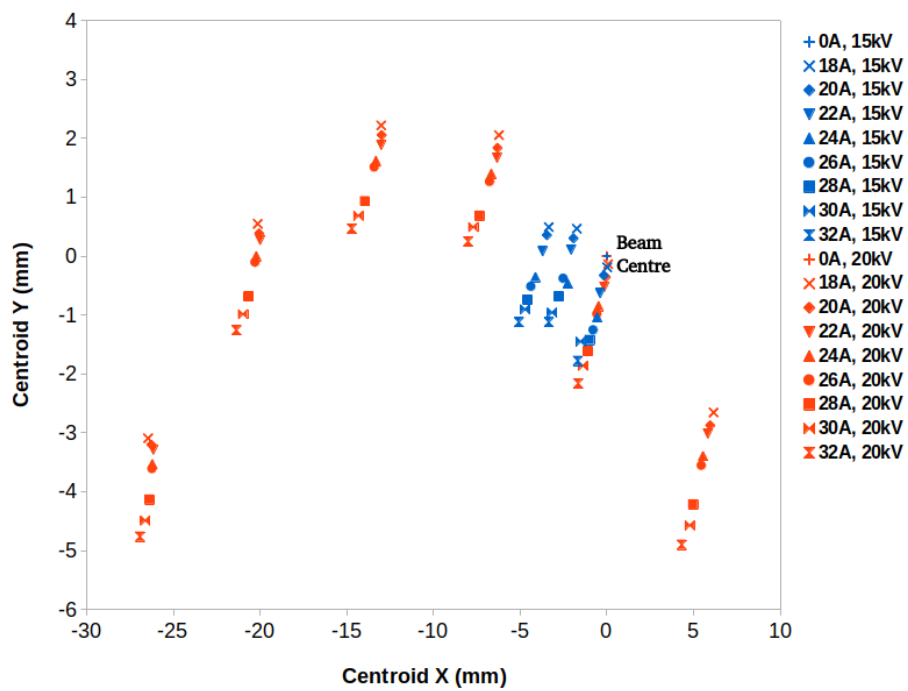
Figure 15. Plot showing Centroid X vs Centroid Y for the 3 spot data with increasing magnetic field strength.
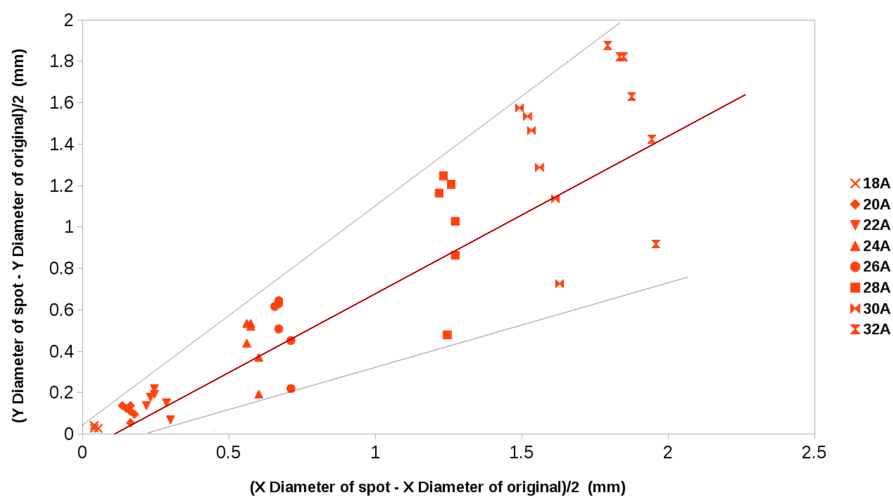

Figure 16. Plot showing variation in X and Y diameter of the 6 spot data with increasing magnetic field strength, compared with no magnetic field.
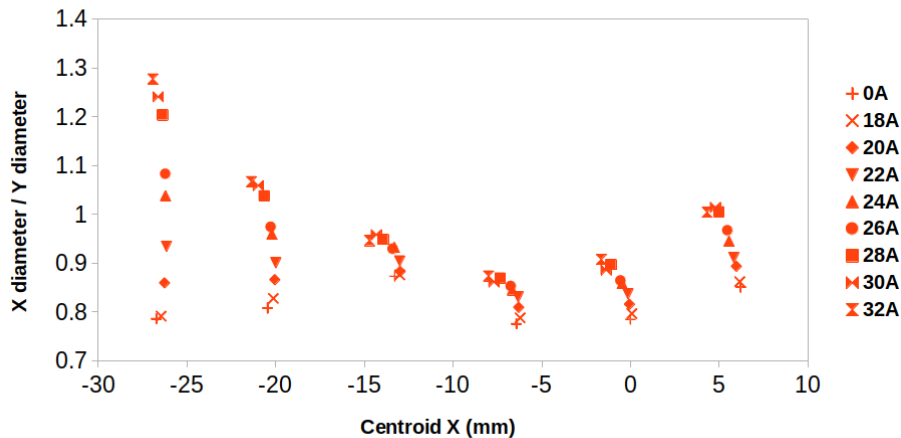
Figure 17. Plot showing ratio of X diameter to Y diameter for beam spots in the 6 spot data with increasing magnetic field strength.

dependent plasma, with the bulk of the plasma shifted radially from the lens centre and rotating around the central axis.

6. Conclusions

We reported and characterised the performance of an electron plasma lens of the Gabor type exposed to a beam of 1.4 MeV protons at the Surrey Proton Beam Centre. Prior measurements at Imperial College indicated that the lens had a stable regime of operation over a range of applied voltages and currents through the coil. During the beam test, the lens was observed to focus pencil beams into rings. The presence of a plasma was confirmed by matching the measured focusing effect with particle transport calculations. An evaluation of the focusing strength showed that the density of the trapped electrons depends on the strength of the radially confining magnetic field, in agreement with the theory. Since the same focusing effects and ring patterns were observed on consecutive days, the plasma instability was associated with the geometry and operation of the lens.

The formation of rings indicates that the plasma column is excited into a coherent off-axis rotation. The size of the rings increases with an increasing current through the coil. A reproducible modulation of the intensity was observed around the circumference of each ring. The position of the centroids of the rings varied non-linearly with the external magnetic field strength, showing a variable plasma trapping efficiency. The X and Y diameters, and the eccentricity of the rings were seen to depend on their position with respect to the beam axis, as a result of the different X and Y focusing forces experienced by each pencil beam.

Both particle-in-cell and particle-tracking simulations showed that a rotation of the bulk of the plasma focuses pencil beams into rings. The size and width of the rings were shown to be determined

by the density of the plasma. Rings with size, eccentricity, and intensity modulation similar to the experimental images were reproduced with a simulation of particle transport through a plasma characterised by the $m = 1$ diocotron instability.

The results described here indicate the presence of a mechanism that drives the rotation of the plasma column. Further investigations are required to identify and describe the exact mechanism that, then, needs to be avoided for the lens to be operated as a reliable focusing device.

7. Acknowledgements

1.   Moehs, D.P.; Peters, J.; Sherman, J. Negative hydrogen ion sources for accelerators. *IEEE Transactions on Plasma Science* **2005**, *33*, 1786–1798. doi:10.1109/TPS.2005.860067.

2.   Lawrie, S. Understanding the plasma and improving extraction of the ISIS Penning H- ions source [PhD thesis]. PhD thesis, University of Oxford, Oxford University Research Archive (ORA), Bodleian Libraries, Osney One, Osney Mead, Oxford OX2 0EW, 2017.

3.   Faircloth, D.; Lawrie, S. An overview of negative hydrogen ion sources for accelerators. *New Journal of Physics* **2018**, *20*, 25007. doi:10.1088/1367-2630/aaa39e.

4.   Tinschert, K.; Iannucci, R.; Lang, R. Electron cyclotron resonance ion sources in use for heavy ion cancer therapy. *Review of Scientific Instruments* **2008**, *79*, 02C505, [https://aip.scitation.org/doi/pdf/10.1063/1.2805226]. doi:10.1063/1.2805226.

5.   Kitagawa, A.; Fujita, T.; Muramatsu, M.; Biri, S.; Drentje, A.G. Review on heavy ion radiotherapy facilities and related ion sources (invited). *Review of Scientific Instruments* **2010**, *81*, 02B909, [https://doi.org/10.1063/1.3268510]. doi:10.1063/1.3268510.

6.   Chao, A.W.; Mess, K.H.; Tigner, M.; Zimmermann, F. *Handbook of Accelerator Physics and Engineering*, 2nd ed.; WORLD SCIENTIFIC, 2013; chapter Subsystems, pp. 543–765. doi:10.1142/9789814415859$_$0007.

7.   Nishiuchi, M.; Daito, I.; Ikegami, M.; Daido, H.; Mori, M.; Orimo, S.; Ogura, K.; Sagisaka, A.; Yogo, A.; Pirozhkov, A.S.; Sugiyama, H.; Kiriyama, H.; Okada, H.; Kanazawa, S.; Kondo, S.; Shimomura, T.; Tanoue, M.; Nakai, Y.; Sasao, H.; Wakai, D.; Sakaki, H.; Bolton, P.; Choi, I.W.; Sung, J.H.; Lee, J.; Oishi, Y.; Fujii, T.; Nemoto, K.; Souda, H.; Noda, A.; Iseki, Y.; Yoshiyuki, T. Focusing and spectral enhancement of a repetition-rated, laser-driven, divergent multi-MeV proton beam using permanent quadrupole magnets. *Applied Physics Letters* **2009**, *94*, 061107, [https://doi.org/10.1063/1.3078291]. doi:10.1063/1.3078291.

8.   Busold, S.; Schumacher, D.; Deppert, O.; Brabetz, C.; Kroll, F.; Blažević, A.; Bagnoud, V.; Roth, M. Commissioning of a compact laser-based proton beam line for high intensity bunches around 10 MeV. *Phys. Rev. ST Accel. Beams* **2014**, *17*, 031302. doi:10.1103/PhysRevSTAB.17.031302.

9.   Bulanov, S.V.; Esirkepov, T.; Khoroshkov, V.S.; Kuznetsov, A.V.; Pegoraro, F. Oncological hadrontherapy with laser ion accelerators. *Physics Letters, Section A: General, Atomic and Solid State Physics* **2002**, *299*, 240–247. doi:10.1016/S0375-9601(02)00521-2.

10.   Malka, V.; Fritzler, S.; Lefebvre, E.; d'Humières, E.; Ferrand, R.; Grillon, G.; Albaret, C.; Meyroneinc, S.; Chambaret, J.P.; Antonetti, A.; Hulin, D. Practicability of protontherapy using compact laser systems. *Medical Physics* **2004**, *31*, 1587–1592, [https://aapm.onlinelibrary.wiley.com/doi/pdf/10.1118/1.1747751]. doi:https://doi.org/10.1118/1.1747751.

11.   Daido, H.; Nishiuchi, M.; Pirozhkov, A.S. Review of laser-driven ion sources and their applications. *Reports on Progress in Physics* **2012**, *75*, 56401. doi:10.1088/0034-4885/75/5/056401.

345   12.   Bin, J.; Allinger, K.; Assmann, W.; Dollinger, G.; Drexler, G.A.; Friedl, A.A.; Habs, D.; Hilz, P.; Hoerlein, R.; Humble, N.; Karsch, S.; Khrennikov, K.; Kiefer, D.; Krausz, F.; Ma, W.; Michalski, D.; Molls, M.; Raith, S.; Reinhardt, S.; Röper, B.; Schmid, T.E.; Tajima, T.; Wenz, J.; Zlobinskaya, O.; Schreiber, J.; Wilkens, J.J. A laser-driven nanosecond proton source for radiobiological studies. *Applied Physics Letters* **2012**, *101*, 243701, [https://doi.org/10.1063/1.4769372]. doi:10.1063/1.4769372.

350   13.   Pozimski, J.; Aslaninejad, M. Gabor lenses for capture and energy selection of laser driven ion beams in cancer treatment. *Laser and Particle Beams* **2013**, *31*, 723–733. doi:10.1017/S0263034613000761.

14.   Pozimski, J.; Aslaninejad, M.; Posocco, P.A. Advanced Gabor Lens Lattice for Laser Driven Hadron Therapy and Other Applications **2016**.

15.   Romano, F.; Schillaci, F.; Cirrone, G.A.P.; Cuttone, G.; Scuderi, V.; Allegra, L.; Amato, A.; Amico, A.; Candiano, G.; De Luca, G.; Gallo, G.; Giordanengo, S.; Guarachi, L.F.; Korn, G.; Larosa, G.; Leanza, R.; Manna, R.; Marchese, V.; Marchetto, F.; Margarone, D.; Milluzzo, G.; Petringa, G.; Pipek, J.; Pulvirenti, S.; Rizzo, D.; Sacchi, R.; Salamone, S.; Sedita, M.; Vignati, A. The ELIMED transport and dosimetry beamline for laser-driven ion beams. *Nuclear Instruments and Methods in Physics Research Section A: Accelerators, Spectrometers, Detectors and Associated Equipment* **2016**, *829*, 153–158. doi:https://doi.org/10.1016/j.nima.2016.01.064.

16.   Aymar, G.; others. The Laser-hybrid Accelerator for Radiobiological Applications. *Front. in Phys.* **2020**, *8*, 567738, [arXiv:physics.acc-ph/2006.00493]. doi:10.3389/fphy.2020.567738.

17.   Zeil, K.; Kraft, S.D.; Bock, S.; Bussmann, M.; Cowan, T.E.; Kluge, T.; Metzkes, J.; Richter, T.; Sauerbrey, R.; Schramm, U. The scaling of proton energies in ultrashort pulse laser plasma acceleration. *New Journal of Physics* **2010**, *12*, 45015. doi:10.1088/1367-2630/12/4/045015.

18.   Prasad, R.; Andreev, A.A.; Ter-Avetisyan, S.; Doria, D.; Quinn, K.E.; Romagnani, L.; Brenner, C.M.; Carroll, D.C.; Dover, N.P.; Neely, D.; Foster, P.S.; Gallegos, P.; Green, J.S.; McKenna, P.; Najmudin, Z.; Palmer, C.A.J.; Schreiber, J.; Streeter, M.J.V.; Tresca, O.; Zepf, M.; Borghesi, M. Fast ion acceleration from thin foils irradiated by ultra-high intensity, ultra-high contrast laser pulses. *Applied Physics Letters* **2011**, *99*, 121504, [https://doi.org/10.1063/1.3643133]. doi:10.1063/1.3643133.

19.   Green, J.S.; Robinson, A.P.L.; Booth, N.; Carroll, D.C.; Dance, R.J.; Gray, R.J.; MacLellan, D.A.; McKenna, P.; Murphy, C.D.; Rusby, D.; Wilson, L. High efficiency proton beam generation through target thickness control in femtosecond laser-plasma interactions. *Applied Physics Letters* **2014**, *104*, 214101, [https://doi.org/10.1063/1.4879641]. doi:10.1063/1.4879641.

375   20.   Dover, N.; Nishiuchi, M.; Sakaki, H.; Kondo, K.; Lowe, H.; Alkhimova, M.; Ditter, E.; Ettlinger, O.; Faenov, A.; Hata, M.; Hicks, G.; Iwata, N.; Kiriyama, H.; Koga, J.; Miyahara, T.; Najmudin, Z.; Pikuz, T.; Pirozhkov, A.; Sagisaka, A.; Schramm, U.; Sentoku, Y.; Watanabe, Y.; Ziegler, T.; Zeil, K.; Kando, M.; Kondo, K. Demonstration of repetitive energetic proton generation by ultra-intense laser interaction with a tape target. *High Energy Density Physics* **2020**, *37*, 100847. doi:10.1016/j.hedp.2020.100847.

380   21.   Margarone, D.; Velyhan, A.; Dostal, J.; Ullschmied, J.; Perin, J.P.; Chatain, D.; Garcia, S.; Bonnay, P.; Pisarczyk, T.; Dudzak, R.; Rosinski, M.; Krasa, J.; Giuffrida, L.; Prokupek, J.; Scuderi, V.; Psikal, J.; Kucharik, M.; De Marco, M.; Cikhardt, J.; Krousky, E.; Kalinowska, Z.; Chodukowski, T.; Cirrone, G.A.P.; Korn, G. Proton Acceleration Driven by a Nanosecond Laser from a Cryogenic Thin Solid-Hydrogen Ribbon. *Phys. Rev. X* **2016**, *6*, 041030. doi:10.1103/PhysRevX.6.041030.

385   22.   Morrison, J.T.; Feister, S.; Frische, K.D.; Austin, D.R.; Ngirmang, G.K.; Murphy, N.R.; Orban, C.; Chowdhury, E.A.; Roquemore, W.M. MeV proton acceleration at kHz repetition rate from ultra-intense laser liquid interaction. *New Journal of Physics* **2018**, *20*, 22001. doi:10.1088/1367-2630/aaa8d1.

23.   Schreiber, J.; Bell, F.; Grüner, F.; Schramm, U.; Geissler, M.; Schnürer, M.; Ter-Avetisyan, S.; Hegelich, B.M.; Cobble, J.; Brambrink, E.; Fuchs, J.; Audebert, P.; Habs, D. Analytical Model for Ion Acceleration by High-Intensity Laser Pulses. *Phys. Rev. Lett.* **2006**, *97*, 045005. doi:10.1103/PhysRevLett.97.045005.

24.   Qiao, B.; Zepf, M.; Borghesi, M.; Geissler, M. Stable GeV Ion-Beam Acceleration from Thin Foils by Circularly Polarized Laser Pulses. *Phys. Rev. Lett.* **2009**, *102*, 145002. doi:10.1103/PhysRevLett.102.145002.

25.   Pozimski, J.; Aslaninejad, M. Gabor lenses for capture and energy selection of laser driven ion beams in cancer treatment. *Laser and Particle Beams* **2013**, *31*, 723–733.

395   26.   Gabor, D. A space-charge lens for the focusing of ion beams. *Nature* **1947**, *160*, 89.

27.   Mobley, R.; Gamml, G.; Maschke, A. Gabor lenses, 1979. BNL–25787.

28. Lefevre, H.W.; Booth, R. Progress in Space Charge Lens Development. *IEEE Transactions on Nuclear Science* **1979**, *26*, 3115–3117.

29. Palkovic, J.; Hren, R.; Lee, G.; Mills, F.E.; Schmidt, C.; Wendt, J.; Young, D. Measurements on a Gabor Lens for Neutralizing and Focusing a 30-KeV Proton Beam. 1988.

30. Tauschwitz, A.; Boggasch, E.; Wetzler, H.; Hoffmann, D.H.H.; Neuner, U.; Stetter, M.; Stöwe, S.; Tkotz, R.; de Magistris, M.; Seelig, W. Plasma lens focusing of heavy ion beams utilizing a wall-stabilized discharge. 1994 10th International Conference on High-Power Particle Beams, 1994, Vol. 2, pp. 695–698.

31. Chekh, Y.M.; Goncharov, A.A.; Protsenko, I.M.; Dobrovolsky, A.M.; Brown, I.G. Electrostatic plasma lens for accelerator injection application. *Review of Scientific Instruments* **2006**, *77*, 03B906, [https://doi.org/10.1063/1.2165577]. doi:10.1063/1.2165577.

32. Dobrovolskiy, A.; Dunets, S.; Evsyukov, A.; Goncharov, A.; Gushenets, V.; Litovko, I.; Oks, E. Recent advances in plasma devices based on plasma lens configuration for manipulating high-current heavy ion beams. *Review of Scientific Instruments* **2010**, *81*, 02B704, [https://doi.org/10.1063/1.3264630]. doi:10.1063/1.3264630.

33. Schulte, K.; Droba, M.; Meusel, O.; Ratzinger, U.; Adonin, A.; Berezov, R.; Hollinger, R.; Pfister, J. Gabor Lens Performance Studies at the GSI High Current Test Injector. Proceedings, 4th International Particle Accelerator Conference (IPAC 2013): Shanghai, China, May 12-17, 2013, 2013, p. THPWO021.

34. Pozimski, J.; Meusel, O. Space charge lenses for particle beams. *Review of scientific instruments* **2005**, *76*, 063308.

35. Pozimski, J.; Aslaninejad, M.; Posocco, P.A. Advanced Gabor Lens Lattice for Laser Driven Hadron Therapy and Other Applications. Proceedings, 7th International Particle Accelerator Conference (IPAC 2016): Busan, Korea, May 8-13, 2016, 2016, p. TUPMY023. doi:10.18429/JACoW-IPAC2016-TUPMY023.

36. Malmberg, J.H.; deGrassie, J.S. Properties of Nonneutral Plasma. *Phys. Rev. Lett.* **1975**, *35*, 577–580. doi:10.1103/PhysRevLett.35.577.

37. Malmberg, J.H.; Driscoll, C.F. Long-Time Containment of a Pure Electron Plasma. *Phys. Rev. Lett.* **1980**, *44*, 654–657. doi:10.1103/PhysRevLett.44.654.

38. Pozimski, J.; Grol, P.; Diilling, R.; Weis, T.; Physik, A.; Wolfgang, D.J.; Main, D.F. First Experimental Studies of a Gabor-Plasma-Lens in Frankfurt. pp. 1536–1538.

39. Chekh, Y.; Goncharov, A.; Protsenko, I.; Brown, I.G. Effect of the electrostatic plasma lens on the emittance of a high-current heavy ion beam. *Applied Physics Letters* **2005**, *86*, 041502, [https://doi.org/10.1063/1.1855428]. doi:10.1063/1.1855428.

40. Meusel, O.; Droba, M.; Glaeser, B.; Schulte, K. Experimental studies of stable confined electron clouds using Gabor lenses. *AIP Conf. Proc. C* **2013**, *1206051*, 157–160. 4 p. Comments: 4 pages, contribution to the Joint INFN-CERN-EuCARD-AccNet Workshop on Electron-Cloud Effects: ECLOUD'12; 5-9 Jun 2012, La Biodola, Isola d'Elba, Italy, doi:10.5170/CERN-2013-002.157.

41. Levy, R.H. Diocotron Instability in a Cylindrical Geometry. *The Physics of Fluids* **1965**, *8*, 1288–1295, [https://aip.scitation.org/doi/pdf/10.1063/1.1761400]. doi:10.1063/1.1761400.

42. Sjobak, K.; Adli, E.; Bergamaschi, M.; Burger, S.; Corsini, R.; Curcio, A.; Curt, S.; Döbert, S.; Farabolini, W.; Gamba, D.; others. Status of the CLEAR electron beam user facility at CERN. 10th Int. Particle Accelerator Conf.(IPAC'19), Melbourne, Australia, 2019.

43. Lindstrøm, C.A.; Adli, E.; Boyle, G.; Corsini, R.; Dyson, A.; Farabolini, W.; Hooker, S.; Meisel, M.; Osterhoff, J.; Röckemann, J.H.; others. Emittance preservation in an aberration-free active plasma lens. *Physical review letters* **2018**, *121*, 194801.

44. Lindstrøm, C.A.; Sjobak, K.; Adli, E.; Röckemann, J.H.; Schaper, L.; Osterhoff, J.; Dyson, A.; Hooker, S.; Farabolini, W.; Gamba, D.; others. Overview of the CLEAR plasma lens experiment. *Nuclear Instruments and Methods in Physics Research Section A: Accelerators, Spectrometers, Detectors and Associated Equipment* **2018**, *909*, 379–382.

45. Joshi, C.; Blue, B.; Clayton, C.; Dodd, E.; Huang, C.; Marsh, K.; Mori, W.; Wang, S.; Hogan, M.; O'Connell, C.; others. High energy density plasma science with an ultrarelativistic electron beam. *Physics of Plasmas* **2002**, *9*, 1845–1855.

46. Hogan, M.J.; Clayton, C.E.; Huang, C.; Muggli, P.; Wang, S.; Blue, B.E.; Walz, D.; Marsh, K.A.; O'Connell, C.L.; Lee, S.; Iverson, R.; Decker, F.J.; Raimondi, P.; Mori, W.B.; Katsouleas, T.C.; Joshi, C.; Siemann, R.H.

Ultrarelativistic-Positron-Beam Transport through Meter-Scale Plasmas. *Phys. Rev. Lett.* **2003**, *90*, 205002. doi:10.1103/PhysRevLett.90.205002.

47. Muggli, P.; Blue, B.; Clayton, C.; Decker, F.; Hogan, M.; Huang, C.; Joshi, C.; Katsouleas, T.C.; Lu, W.; Mori, W.; others. Halo formation and emittance growth of positron beams in plasmas. *Physical review letters* **2008**, *101*, 055001.

48. van Tilborg, J.; Steinke, S.; Geddes, C.G.R.; Matlis, N.H.; Shaw, B.H.; Gonsalves, A.J.; Huijts, J.V.; Nakamura, K.; Daniels, J.; Schroeder, C.B.; Benedetti, C.; Esarey, E.; Bulanov, S.S.; Bobrova, N.A.; Sasorov, P.V.; Leemans, W.P. Active Plasma Lensing for Relativistic Laser-Plasma-Accelerated Electron Beams. *Phys. Rev. Lett.* **2015**, *115*, 184802. doi:10.1103/PhysRevLett.115.184802.

49. van Tilborg, J.; Barber, S.K.; Tsai, H.E.; Swanson, K.K.; Steinke, S.; Geddes, C.G.R.; Gonsalves, A.J.; Schroeder, C.B.; Esarey, E.; Bulanov, S.S.; Bobrova, N.A.; Sasorov, P.V.; Leemans, W.P. Nonuniform discharge currents in active plasma lenses. *Phys. Rev. Accel. Beams* **2017**, *20*, 032803. doi:10.1103/PhysRevAccelBeams.20.032803.

50. Doss, C.E.; Adli, E.; Ariniello, R.; Cary, J.; Corde, S.; Hidding, B.; Hogan, M.J.; Hunt-Stone, K.; Joshi, C.; Marsh, K.A.; others. Laser-ionized, beam-driven, underdense, passive thin plasma lens. *Physical Review Accelerators and Beams* **2019**, *22*, 111001.

51. Barov, N.; Conde, M.E.; Gai, W.; Rosenzweig, J.B. Propagation of Short Electron Pulses in a Plasma Channel. *Phys. Rev. Lett.* **1998**, *80*, 81–84. doi:10.1103/PhysRevLett.80.81.

52. Pompili, R.; Anania, M.P.; Bellaveglia, M.; Biagioni, A.; Bini, S.; Bisesto, F.; Brentegani, E.; Castorina, G.; Chiadroni, E.; Cianchi, A.; Croia, M.; Di Giovenale, D.; Ferrario, M.; Filippi, F.; Giribono, A.; Lollo, V.; Marocchino, A.; Marongiu, M.; Mostacci, A.; Di Pirro, G.; Romeo, S.; Rossi, A.R.; Scifo, J.; Shpakov, V.; Vaccarezza, C.; Villa, F.; Zigler, A. Experimental characterization of active plasma lensing for electron beams. *Applied Physics Letters* **2017**, *110*, 104101, [https://doi.org/10.1063/1.4977894]. doi:10.1063/1.4977894.

53. Chiadroni, E.; others. Overview of Plasma Lens Experiments and Recent Results at SPARC_LAB. *Nucl. Instrum. Meth. A* **2018**, *909*, 16–20, [arXiv:physics.acc-ph/1802.00279]. doi:10.1016/j.nima.2018.02.014.

54. Pompili, R.; Chiadroni, E.; Cianchi, A.; Del Dotto, A.; Faillace, L.; Ferrario, M.; Iovine, P.; Masullo, M.R. Plasma lens-based beam extraction and removal system for Plasma Wakefield Acceleration experiments. *Phys. Rev. Accel. Beams* **2019**, *22*, 121302, [arXiv:physics.acc-ph/1909.01001]. doi:10.1103/PhysRevAccelBeams.22.121302.

55. Dotto, A.D.; Chiadroni, E.; Cianchi, A.; Faillace, L.; Ferrario, M.; Iovine, P.; Masullo, M.R.; Pompili, R. Compact and tunable active-plasma lens system for witness extraction and driver removal. Journal of Physics: Conference Series. IOP Publishing Ltd, 2020, Vol. 1596, p. 012050. doi:10.1088/1742-6596/1596/1/012050.

56. Danielson, J.R.; Weber, T.R.; Surko, C.M. Plasma manipulation techniques for positron storage in a multicell trap. *Physics of Plasmas* **2006**, *13*, 123502, [https://doi.org/10.1063/1.2390690]. doi:10.1063/1.2390690.

57. Hurst, N.C.; Danielson, J.R.; Baker, C.J.; Surko, C.M. Confinement and manipulation of electron plasmas in a multicell trap. *Physics of Plasmas* **2019**, *26*, 013513, [https://doi.org/10.1063/1.5078649]. doi:10.1063/1.5078649.

58. University of Surrey Ion Beam Centre. https://www.surrey.ac.uk/ion-beam-centre. Accessed: 2021-01-19.

59. Neuner, U.; Bock, R.; Roth, M.; Spiller, P.; Constantin, C.; Funk, U.N.; Geissel, M.; Hakuli, S.; Hoffmann, D.H.H.; Jacoby, J.; Kozyreva, A.; Tahir, N.A.; Udrea, S.; Varentsov, D.; Tauschwitz, A. Shaping of Intense Ion Beams into Hollow Cylindrical Form. *Phys. Rev. Lett.* **2000**, *85*, 4518–4521. doi:10.1103/PhysRevLett.85.4518.

60. Posocco, P.A.; Merchant, M.; Pozimski, J.; Xia, Y. First Test of The Imperial College Gabor (Plasma) Lens prototype at the Surrey Ion Beam centre. Proceedings, 7th International Particle Accelerator Conference (IPAC 2016): Busan, Korea, May 8-13, 2016, 2016, p. TUPMY024. doi:10.18429/JACoW-IPAC2016-TUPMY024.

61. VSim for Plasma, 2020. https://www.txcorp.com/vsim.

62. Kapetanakos, C.A.; Hammer, D.A.; Striffler, C.D.; Davidson, R.C. Destructive Instabilities in Hollow Intense Relativistic Electron Beams. *Phys. Rev. Lett.* **1973**, *30*, 1303–1306. doi:10.1103/PhysRevLett.30.1303.

63. Rosenthal, G.; Dimonte, G.; Wong, A.Y. Stabilization of the diocotron instability in an annular plasma. *The Physics of Fluids* **1987**, *30*, 3257–3261, [https://aip.scitation.org/doi/pdf/10.1063/1.866501]. doi:10.1063/1.866501.

64. Levy, R.H. Diocotron Instability in a Cylindrical Geometry. *The Physics of Fluids* **1965**, *8*, 1288–1295, [https://aip.scitation.org/doi/pdf/10.1063/1.1761400]. doi:10.1063/1.1761400.

65. Nevay, L.J.; others. BDSIM: An accelerator tracking code with particle-matter interactions. *Computer Physics Communications* **2020**, p. 107200.

505